



Oxidation of residual methane from VNG vehicles over Co_3O_4 -based catalysts: Comparison among bulk, Al_2O_3 -supported and Ce-doped catalysts

Andoni Choya, Beatriz de Rivas, Juan Ramón González-Velasco, Jose Ignacio Gutiérrez-Ortiz, Rubén López-Fonseca*

Chemical Technologies for Environmental Sustainability Group, Department of Chemical Engineering, Faculty of Science and Technology, University of the Basque Country UPV/EHU, PO Box 644, E-48080, Bilbao, Spain

ARTICLE INFO

Keywords:

Catalytic combustion
Methane
Cobalt oxide
Cerium doping
Oxygen mobility

ABSTRACT

Cobalt oxide based catalysts with three different active phase configurations, namely bulk, alumina supported and cerium-doped Co_3O_4 samples were examined for the complete oxidation of methane under conditions similar to those found in the exhaust of VNG engines. The structural and redox properties of the resulting catalysts were determined by N_2 adsorption-desorption, WDXRF, ICP-AES, X-Ray diffraction, temperature-programmed reactions, UV-vis-NIR DRS, XPS and Raman spectroscopy. Alumina-supported catalysts (10–40%wt. Co) were found to be less active, since the strong interactions between the alumina and the Co_3O_4 active phase were highly detrimental for the redox properties of these catalysts. On the other hand, doping with cerium (10%wt.) led to an increased inherent activity of the Co_3O_4 phase by distorting the spinel lattice, which resulted in improved structural and redox properties and enhanced mobility of the oxygen species within the spinel lattice. These catalysts were also stable over a prolonged period of time under both dry and humid conditions (150 h).

1. Introduction

The use of natural gas as fuel for vehicles (also known as Vehicular Natural Gas or VNG) is considered a reliable alternative, with a well-established technology, that can serve as a transition technology in the way to cleaner H_2 -based energy sources. VNG engines are between 10–20% more efficient than gasoline or diesel engines and have a lower environmental impact with limited NO_x and soot emissions [1–4]. Their main technical limitation lies in the release of residual methane, not burned in the engine, which is a powerful greenhouse effect gas.

Catalytic oxidation constitutes an attractive post-treatment strategy to convert methane into CO_2 and water. Unfortunately, it is a noticeably demanding process compared with the oxidation of other hydrocarbons such as propane or butane, due to its high chemical stability. This low reactivity determines the temperature of the process, which should not exceed a temperature threshold of 500 °C, since that is the thermal level of the exhaust gases from the engine. The mostly used catalysts on a commercial scale for VNG vehicles are based on supported noble metals, mainly palladium [5,6]. However, these catalysts, which can contain up to a 4% in weight of palladium, are expensive while their behaviour is negatively influenced by sintering and the presence of water in the reaction stream [7,8]. In this context, finding cheaper, alternative catalysts with an appropriate performance has become an

interesting challenge that has the potential to reduce the cost of post-treatment systems for exhaust gases and contribute to increase the attractiveness of VNG engines as well.

Cobalt spinel oxides, like Co_3O_4 , have been demonstrated to exhibit a high activity for methane catalytic combustion, and are therefore considered good alternative candidates to noble metal based catalysts, owing to their relatively low cost, high thermal and hydrothermal stability and selectivity to CO_2 [9,10]. However, the specific physico-chemical properties of these catalysts are highly dependent on the specific configuration of the active phase, that is, whether the Co_3O_4 is a bulk phase, supported on a porous media, or mixed with other elements. Pure bulk Co_3O_4 catalysts take advantage of the excellent redox properties of this material, which allow for a good mobility of the oxygen species and reducibility. However, their structural properties are usually very poor when using conventional synthesis methodologies (precipitation or direct calcination), with low specific surface areas and large crystallite sizes [11,12]. Better textural properties can be obtained with solvothermal or hard-template-based routes [13–16]. In a simpler way, an increased available metallic surface area and improved structural properties can be obtained by depositing the Co_3O_4 phase over the surface of a porous media. This strategy has been reported to enhance the inherent catalytic activity of Co_3O_4 in some cases [17,18], but, in other cases, the interactions between cobalt oxide and the support can

* Corresponding author.

E-mail address: ruben.lopez@ehu.es (R. López-Fonseca).

be detrimental owing to their negative impact on the redox properties [19]. For example, when alumina is used as a support the formation of CoAl_2O_4 often occurs. This undesired phase fixes a certain amount of cobalt species due to its high stability. Therefore, a fraction of deposited cobalt species is not able to participate in the $\text{Co}^{3+}/\text{Co}^{2+}$ redox cycle. On the other hand, doping the bulk Co_3O_4 with another metallic element can improve its textural and redox properties [20,21]. The properties of the resultant catalysts strongly depend on various parameters such as the composition or the presence of segregated or undesired phases [22].

Up to now, various cobalt-based catalysts with the described three configurations have been profusely examined for the complete oxidation of methane [9,17,23–28]. However, the different routes employed for catalysts synthesis and the wide range of operation conditions chosen for catalytic evaluation make the comparison of their corresponding performance and properties a particularly difficult task [29]. To the best of our knowledge, no systematic analysis of the three type of catalysts under the same conditions has ever been attempted. Thus, in the present work, these three configurations have been implemented for the design of Co_3O_4 catalysts for methane catalytic oxidation. More specifically, various bulk Co_3O_4 samples were prepared by simple calcination and precipitation. Secondly, a series of Co_3O_4 catalysts supported on alumina with varying cobalt content in the range 10–40%wt. were examined. Lastly, as for doped Co_3O_4 catalysts, several samples modified by cerium, with a content between 5 and 20%wt., were synthesised. Along with a detailed characterisation of the physicochemical properties of these catalysts, by means of a wide number of analytical techniques including BET measurements, XRD, WDXRF, ICP-AES, UV–vis-NIR DRS, Raman spectroscopy, XPS, H_2 -TPR and CH_4 -TPRe, this work presents kinetic data that were correlated with the key catalytic properties of each type of catalyst. Also, attention has been paid to examining the catalytic stability during a prolonged time interval under both dry and humid conditions.

2. Experimental

2.1. Catalysts preparation

Bulk Co_3O_4 catalysts were prepared following two different routes, already described elsewhere [30]. The first route was a simple calcination in static air of two different cobalt precursors, namely cobalt (II) nitrate hexahydrate ($\text{Co}(\text{NO}_3)_2 \cdot 6\text{H}_2\text{O}$, Sigma-Aldrich) and cobalt (II) hydroxycarbonate ($2\text{CoCO}_3 \cdot 3\text{Co}(\text{OH})_2 \cdot x\text{H}_2\text{O}$, Panreac). The resulting samples were denoted as DC and HC, respectively. The second route consisted of an aqueous basic precipitation of a cobalt precursor, resulting in the formation of cobalt hydroxycarbonate. A solution of Na_2CO_3 1.2 M was added drop-by-drop to 100 ml of $\text{Co}(\text{NO}_3)_2 \cdot 6\text{H}_2\text{O}$ 0.5 M, while the temperature was kept constant at 80 °C, until pH 8.5 was attained. The obtained precipitates were collected and washed thoroughly with at least 5 litres of water, to wash off all the sodium ions which are known to be especially detrimental for the activity of oxidation catalysts [31]. The sample was labelled as CC. Finally, a commercial bulk Co_3O_4 sample (Alfa Aesar) was used as reference. This sample was denoted as COM.

Supported $\text{Co}_3\text{O}_4/\text{Al}_2\text{O}_3$ catalysts were prepared by a precipitation route following the same methodology as the CC catalyst, but adding γ - Al_2O_3 (Saint Gobain Norpro SA 6173), previously stabilized at 850 °C for 4 h in static air. The selected metallic Co loadings were 10, 20, 30, 35 and 40 wt%. These samples were denoted as $x\text{Co}/\text{Al}_2\text{O}_3$ where x stands for the nominal cobalt loading. For comparative purposes, a bulk CoAl_2O_4 sample was also obtained by a precipitation route, where a cobalt salt ($\text{Co}(\text{NO}_3)_2 \cdot 6\text{H}_2\text{O}$) and an aluminium salt ($\text{Al}(\text{NO}_3)_3 \cdot 9\text{H}_2\text{O}$) with stoichiometric proportions were precipitated by the drop-by-drop addition of Na_2CO_3 1.2 M, until pH 9 was achieved.

Cerium-doped bulk Co_3O_4 catalysts were prepared by a precipitation route, similar to the route followed for the synthesis of the CC

sample, but starting from adjusted mixtures of $\text{Ce}(\text{NO}_3)_3 \cdot 6\text{H}_2\text{O}$ and $\text{Co}(\text{NO}_3)_2 \cdot 6\text{H}_2\text{O}$ to obtain catalysts with nominal cerium loadings of 5, 10, 15 and 20 wt%, which corresponded to Ce/Co molar ratios of 0.03, 0.06, 0.10 and 0.14, respectively. The samples were named as $x\text{Ce}/\text{Co}_3\text{O}_4$ where x is the nominal cerium content. In addition, a sample of pure CeO_2 was prepared using the same route. Again, the obtained precipitates were collected and washed thoroughly with water. All catalyst precursors were dried in static air at 110 °C for 16 h and subjected to calcination in static air to produce the final catalysts. The calcination protocol was defined on the basis of the results obtained from a previous thermogravimetric analysis over the catalyst precursors, and involved three heating steps, separated by 30-minute isotherms: an initial step at 5 °C min⁻¹ from room temperature to 125 °C, an intermediate step at 1 °C min⁻¹ until 300 °C and a final step at 5 °C min⁻¹ until 600 °C, which was then maintained for 4 h. Exceptionally, the bulk CoAl_2O_4 sample was also calcined at 850 °C.

2.2. Characterisation techniques

Textural properties of the catalysts were determined from the nitrogen-adsorption isotherms at –196 °C obtained with a Micromeritics TriStar II apparatus. The specific surface of the samples was obtained by the BET method, and the average pore size was calculated using the BJH method. All samples were degassed prior to analysis on a Micromeritics SmartPrep apparatus at 300 °C for 10 h with a N_2 flow.

The composition of the supported $\text{Co}_3\text{O}_4/\text{Al}_2\text{O}_3$ catalysts and the CoAl_2O_4 samples was determined by Wavelength Dispersive X-Ray Fluorescence (WDXRF). From each sample in powder form, a boron glass pearl was prepared by fusion in an induction micro-furnace, by mixing the sample with the flux agent Spectromelt A12 (Merck) in an approximate proportion of 20:1. Chemical analysis of each pearl was performed under vacuum, using a PANalytical AXIOS sequential WDXRF spectrometer, equipped with a Rh tube and three different detectors (gas flow, scintillation and Xe sealed). The composition of Ce-doped catalysts was determined by ICP-AES in a Thermo Elemental Iris Intrepid apparatus. The pretreatment involved the acid digestion of 5–10 mg of each sample, followed by dissolution in 100 ml of Milli-Q water.

Structural properties of the catalysts were determined by X-Ray diffraction. XRD analysis were performed on a X'PERT-PRO X-Ray diffractometer using $\text{Cu K}\alpha$ radiation ($\lambda = 1.5406 \text{ \AA}$) and a Ni filter. The X-Ray tube was operated at 40 kV and 40 mA of current. The samples were scanned from an initial value of $2\theta = 5^\circ$ to a final value of $2\theta = 80^\circ$, with a step size of 0.026° and a counting time of 2.0 s for each step. Phase identification was performed by comparison of the obtained diffraction patterns with JCPDS (Joint Committee on Powder Diffraction Standards) database cards. Occasionally, a longer counting time (26.8 s) was applied to perform a detailed XRD analysis over the supported $\text{Co}_3\text{O}_4/\text{Al}_2\text{O}_3$ and Ce-doped catalysts. The cell size of the Co_3O_4 phase was obtained by profile matching of the detailed XRD patterns using FullProf.2k software.

Redox properties and Co species distribution was investigated by means of different techniques. Temperature-programmed reduction with hydrogen (H_2 -TPR) was performed on a Micromeritics Autochem 2920 apparatus, using a 5% H_2 /Ar mixture as the reducing gas. The analysis protocol involved an initial pre-treatment step with a 5% O_2 /He mixture at 300 °C for 30 min. The aim of this step was to remove impurities and/or water that could be retained on the surface of the samples while at the same time fully restoring the oxygen vacancies of the spinel lattice before the analysis of the reducibility. After cooling down to room temperature with flowing He, the TPR experiment was performed, up to 600 °C for the bulk Co_3O_4 catalysts, 950 °C for the supported $\text{Co}_3\text{O}_4/\text{Al}_2\text{O}_3$ catalysts and CoAl_2O_4 samples and 900 °C for the Ce-doped Co_3O_4 catalysts. The corresponding final temperature was then maintained for 30 min. The water produced throughout the whole experiment was eliminated using a cold trap, to avoid interference with

Table 1
Physicochemical characterisation of bulk Co_3O_4 catalysts.

Catalyst	S_{BET} , $\text{m}^2 \text{g}^{-1}$	V_p , $\text{cm}^3 \text{g}^{-1}$	D_p , \AA	$D_{\text{Co}_3\text{O}_4}$, nm	Low-temperature H_2 uptake, mmol g^{-1}	High-temperature H_2 uptake, mmol g^{-1}	Relative H_2 uptake at low and high temperature	$\text{Co}^{3+}/\text{Co}^{2+}$ (XPS)	$\text{O}_{\text{ads}}/\text{O}_{\text{latt}}$ (XPS)
CC	14	0.09	257	63	4.3	12.4	0.35	1.96	0.40
HC	12	0.06	350	64	4.0	12.3	0.33	1.70	0.49
DC	5	0.02	353	84	3.9	12.8	0.30	1.50	0.57
COM	8	0.03	412	75	4.1	12.3	0.33	1.76	0.49

the TCD detector. Additional information regarding the reducibility of the catalysts was obtained by means of temperature programmed reaction with a 5% CH_4 /He mixture in the absence of oxygen (CH_4 -TPRe) coupled to mass spectrometry (MKS Cirrus Quadrupole Mass Spectrometer).

X-Ray photoelectron spectroscopy (XPS) analysis was performed using a SPECS system equipped with a Phoibos 150 1D analyzer and a DLD-monochromatic radiation source. UV-vis-NIR diffuse reflectance (DRS) spectra of the samples was obtained on a Jasco V-570 apparatus in the 200–2300 nm wavelength range. The analysis by Raman spectroscopy was carried out by using a Renishaw InVia Raman spectrometer, coupled to a Leica DMLM microscope. The excitation wavelength was 514 nm (ion-argon laser, Modu-Laser). The spatial resolution was 2 microns. For each spectrum 20 s were employed and 5 scans were accumulated with the 10% of the maximum power of the 514 nm laser in a spectral window of 150–1200 cm^{-1} .

2.3. Catalytic activity determination

Catalytic activity tests were performed in a bench-scale fixed bed reactor, Microactivity modular laboratory system manufactured by PID Eng&Tech S.L., operated at atmospheric pressure and monitored by computer. The reactor was a stainless steel (Hastelloy X) tube, manufactured by Autoclave Engineers, with an internal diameter of 8.55 mm and a length of 305 mm. The temperature inside the reactor was measured by a multipoint K type thermocouple placed in the catalyst bed. For each reaction experiment, 1 g of catalyst granulated to a particle size of 0.25–0.3 mm was loaded into the reactor, diluted with 1 g of inert quartz granulated to a particle size of 0.5–0.8 mm to improve gas flow and heat distribution along the bed and avoid diffusional effects affecting the reaction rate. A reactor diameter/particle diameter ratio (31) higher than 10 and a catalytic bed length/particle diameter ratio (79) higher than 50 ensured that both by-pass and axial dispersion effects could be neglected (Table S1, Supplementary material). Thus, an ideal plug-flow in the reactor could be supposed.

The feed consisted of a gaseous mixture of 1% CH_4 , 10% O_2 and N_2 as the balance gas. The selected composition of the gas feed was comparable to that found in the exhaust of VNG engines, which typically contains 0.5–1% CH_4 and 5–10% O_2 . A total gas flow of 500 $\text{cm}^3 \text{min}^{-1}$ was used, which corresponded to a gas hourly space velocity of 60,000 h^{-1} approximately (300 $\text{ml CH}_4 \text{g}^{-1} \text{h}^{-1}$). Catalytic activity was measured from 200 to 600 °C. Conversion measurements and product profiles were taken at steady state each 25 °C, typically after 15 min on stream. The furnace temperature was programmed in a stepwise progression. Each temperature level was attained using a heating ramp of 1 °C min^{-1} . Additionally, stability tests (1% CH_4 , 10% O_2 and N_2 as the balance gas) in the presence (10% H_2O) or absence of water vapour were carried out for a total time on stream of 150 h at 450 °C. Methane conversion was calculated by the difference between inlet and outlet CH_4 concentrations. Inlet and outlet streams were analysed using an on-line Agilent Technologies 7890 N gas chromatograph equipped with a thermal conductivity detector (TCD) and two columns: a PLOT 5 A molecular sieve column for the analysis of CH_4 , O_2 , N_2 and CO ; and a PLOT U column for CO_2 analysis. Each chromatographic analysis was performed in triplicate in order to check reproducibility, which was

below 1%. To ensure that the obtained catalytic results were not affected by both mass and heat transfer limitations, the criteria for intra-granular and extra-granular mass diffusion, energy diffusion and temperature gradients were checked to be above the limit, according to the Eurokin procedure [32,33]. It was therefore considered that catalytic activity results were not significantly influenced by interphase transportation. The calculations are summarised in Table S1 (Supplementary material).

3. Results and discussion

3.1. Evaluation of bulk Co_3O_4 catalysts

The textural properties of the bulk Co_3O_4 samples in terms of BET surface area, pore mean diameter and pore volume are shown in Table 1. The surface area varied between 5 $\text{m}^2 \text{g}^{-1}$ over the DC sample and 14 $\text{m}^2 \text{g}^{-1}$ over the CC sample. This latter oxide also exhibited the largest pore volume and smallest pore diameter, thus suggesting that the CC route produces samples with better textural properties. The structural properties were characterised by XRD, using the JCDPS files as a reference. For every sample, all diffraction peaks, located at 19.0°, 31.3°, 36.8°, 44.8°, 59.4° and 65.2°, could be assigned to a pure phase of mixed cobalt (II,III) oxide with spinel structure (JCPDS 42-1467). The crystallite size, also included in Table 1, was estimated from the Full Width Half Maximum (FWHM) of the characteristic peak located at 36.8°, which corresponded to the (311) plane, by applying the Scherrer equation. It was found that the crystallite sizes, in the 63–84 nm range, inversely correlated to their specific surface area. This relationship was explained in terms of small Co_3O_4 crystallites exposing higher surfaces than larger ones [34,35].

The redox properties of Co_3O_4 were investigated by means of H_2 -TPR. For all samples the hydrogen consumption profiles (Fig. 1) were relatively similar, showing a two-step reduction process. The first

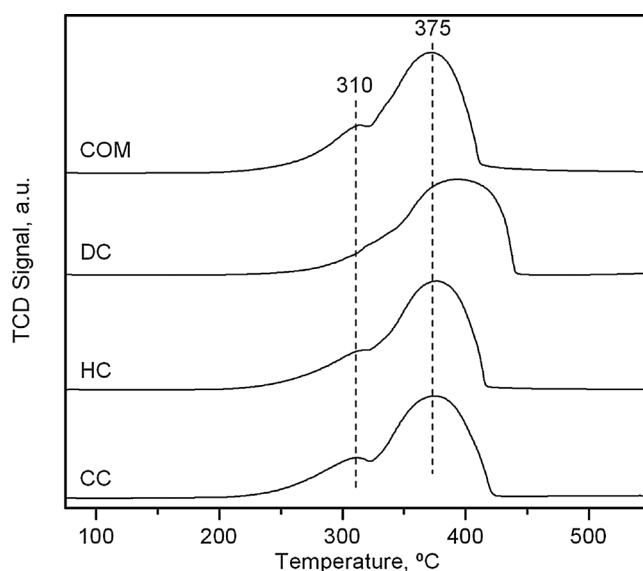


Fig. 1. H_2 -TPR profiles of the bulk Co_3O_4 catalysts.

hydrogen consumption peak, centred at 310 °C, was assigned to the reduction of Co^{3+} to Co^{2+} ; whilst the second reduction peak, located between 325 and 425 °C, was attributed to the reduction of Co^{2+} to metallic Co [36]. No other hydrogen consumption was detected over 500 °C. It was therefore confirmed that the only reducible phase present in all samples was Co_3O_4 . After integration and quantitative evaluation of the TPR profiles, the specific hydrogen uptake of each reduction step and the corresponding ratio were computed, as shown in Table 1. The specific consumption of the synthesised oxides was very similar to the theoretical value (16.6 mmol g^{-1}). As for the ratio between the two uptakes, the CC sample gave the highest value (0.35). This was slightly higher than the theoretical ratio (0.33)

On the other hand, XPS analysis could provide useful information about the distribution of the reducible species on the surface of the spinel. For all bulk Co_3O_4 samples, Co 2p spectra (Fig. S1, Supplementary material) showed broad signals, thus suggesting the presence of various cobalt species on the surface. In particular, the Co $2p_{3/2}$ signal could be deconvoluted in at least five different contributions [37,38]. Hence, the two signals located at lower binding energies, namely 779.5 and 780.7 eV, were attributed to Co^{3+} and Co^{2+} cations associated with oxide O^{2-} anions, respectively, while the signal centred at about 782.7 eV was attributed to the presence of CoO species on the surface. The presence of this species was comparable on the four samples, around 5–10% of the total amount of cobalt. Finally, the two signals located at higher binding energies (785.5 and 789.5 eV) were identified as the satellite signals from Co^{2+} and Co^{3+} ions, respectively [39]. The O 1s spectra showed two different signals located at 529.8 and 530.8 eV, respectively. The former was assigned to oxygen ions from the lattice (O_{latt}) while the latter was attributed to adsorbed oxygen species on the surface (O_{ads}) [40]. From the quantification of the signals, the $\text{Co}^{3+}/\text{Co}^{2+}$ and $\text{O}_{\text{ads}}/\text{O}_{\text{latt}}$ molar ratios (Table 1) could be calculated. The relationship shown in Fig. 2 evidenced that the higher the surface $\text{Co}^{3+}/\text{Co}^{2+}$ molar ratio, the higher the concentration of lattice oxygen species [37].

The catalytic activity of each bulk Co_3O_4 catalyst for the complete oxidation of methane was assessed by defining their respective light-off curves. Since the calcination process would stabilize the catalysts up to the calcination temperature, light-off curves were taken between 200 and 600 °C. For each sample, three consecutive tests were performed. In

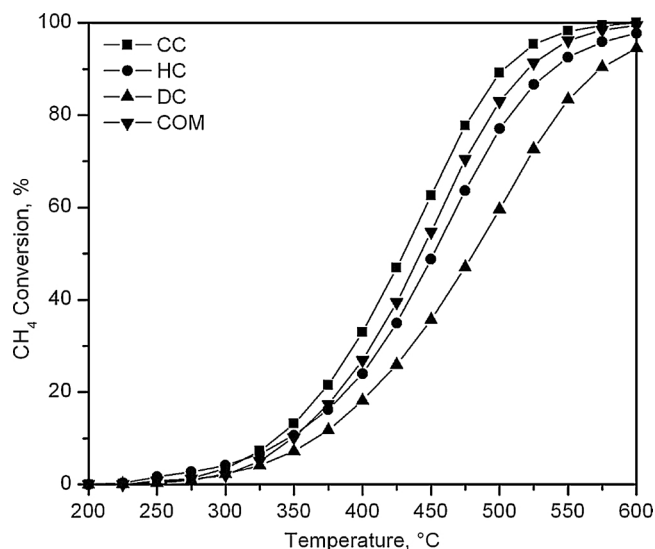


Fig. 3. Light-off curves of the bulk Co_3O_4 catalysts.

all cases, the second and third cycles were characterised by an identical light-off curve (Fig. 3). This revealed that the first cycle worked as a ‘conditioning’ cycle and, after that, the catalysts became stable under the employed reaction conditions. On the basis of the T_{50} (temperature required for 50% conversion) values the following trend was noticed: $\text{CC} > \text{COM} > \text{HC} > \text{DC}$. This finding evidenced that precipitation was a more suitable preparation methodology for bulk oxides. Note that in all cases the selectivity to CO_2 was 100%. The reaction rate of the catalysts was calculated at 375 °C under differential conditions, this is to say, when the methane conversion was below 20%. The estimated values were in the $1.07\text{--}1.85 \text{ mmol CH}_4 \text{ g}_{\text{Co}}^{-1} \text{ h}^{-1}$ range (Table 2). On the other hand, the integral method was applied to estimate the apparent activation energy when considering a first pseudo-order for methane and a zero pseudo-order for oxygen. The assumed reaction orders were compatible with Mars–van Krevelen kinetics with an excess of oxygen, which has already been proven to be the most plausible model for the catalytic oxidation of methane and other hydrocarbons [18,41]. Conversions between 10 and 90% were fit to the following linearized equation for the integral reactor (Eq. (1))

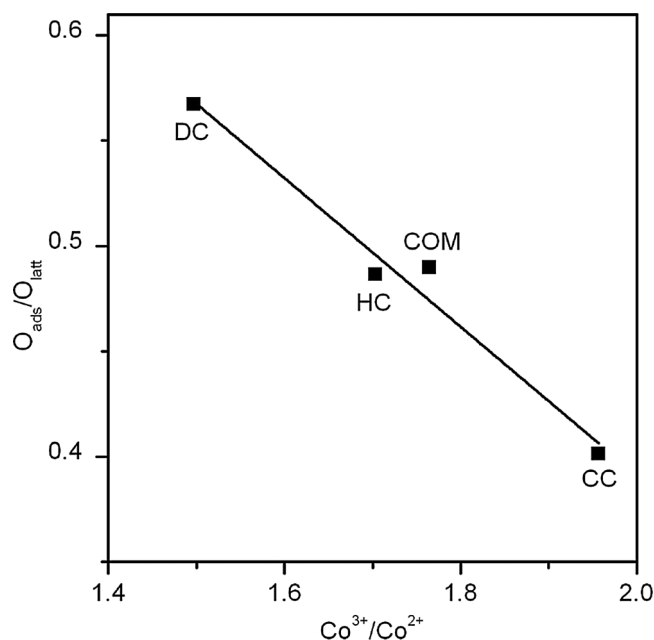


Fig. 2. Relationship between the $\text{Co}^{3+}/\text{Co}^{2+}$ and $\text{O}_{\text{ads}}/\text{O}_{\text{latt}}$ molar ratios of the bulk Co_3O_4 catalysts.

Table 2
Kinetic results of all cobalt catalysts.

Catalyst	T_{10} , °C	T_{50} , °C	T_{90} , °C	Reaction rate, $\text{mmol CH}_4 \text{ g}_{\text{Co}}^{-1} \text{ h}^{-1}$	E_a , kJ mol^{-1}
CC	335	430	505	1.85 ^a	74
HC	355	455	540	1.46 ^a	74
DC	365	480	575	1.07 ^a	74
COM	350	440	520	1.70 ^a	71
10Co/Al ₂ O ₃	510	> 600	> 600	1.17 ^b	100
20Co/Al ₂ O ₃	485	580	> 600	1.17 ^b	92
30Co/Al ₂ O ₃	440	550	> 600	1.87 ^b	80
35Co/Al ₂ O ₃	410	515	575	2.23 ^b	78
40Co/Al ₂ O ₃	350	440	520	2.12 ^b	79
CeO ₂	> 600	> 600	> 600	–	108
5Ce/Co ₃ O ₄	340	435	515	1.81 ^a	78
10Ce/Co ₃ O ₄	340	425	495	2.04 ^a	79
15Ce/Co ₃ O ₄	340	435	500	1.97 ^a	79
20Ce/Co ₃ O ₄	350	435	495	1.90 ^a	85

^a Reaction rate calculated at 375 °C under differential conditions, methane conversion was below 20% over this set of Co_3O_4 -based catalysts.

^b Reaction rate calculated at 425 °C under differential conditions, methane conversion was below 20% over this set of Co_3O_4 -based catalysts.

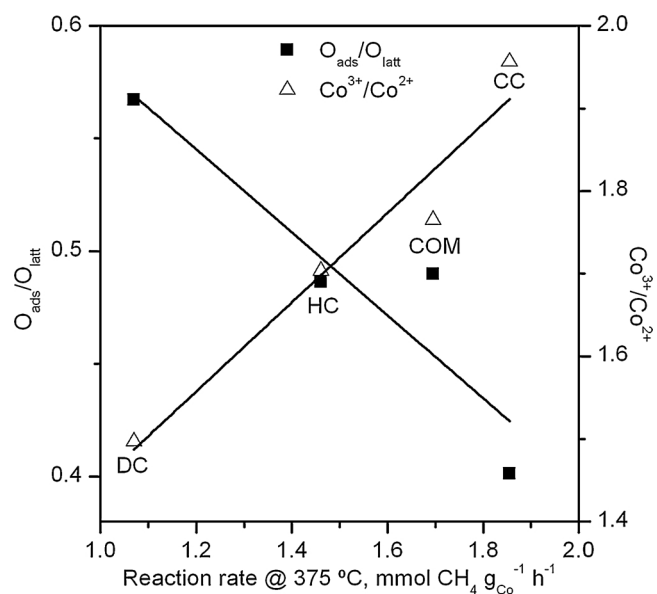


Fig. 4. Relationship among the specific reaction rate and the $\text{Co}^{3+}/\text{Co}^{2+}$ and $\text{O}_{\text{ads}}/\text{O}_{\text{latt}}$ molar ratios of the bulk Co_3O_4 catalysts.

$$\ln[-\ln(1-X)] = \ln \left[k_0 C_{\text{CH}_4} \left(\frac{W}{F_{\text{CH}_4}} \right) \right] - \frac{E_a}{RT} \quad (1)$$

where X is the fractional conversion of methane, k_0 is the pre-exponential factor of the Arrhenius equation and W/F_{CH_4} is the weight hourly space velocity. The goodness of the numerical fit is shown in Fig. S2 (Supplementary material) while the corresponding values for the apparent activation energy for each sample are listed in Table 2. Note that the observed values of the activation energies should be characterized as tentative since effect of the adsorption-desorption equilibrium of the formed water would be hidden into the reported value.

The activation energy of all pure Co_3O_4 samples were very similar ($71\text{--}74 \text{ kJ mol}^{-1}$) and comparable with the values reported in the literature for this reaction [42,43]. On the other hand, Fig. 4 revealed that there was a good correlation between the reaction rate at 375°C and the surface $\text{Co}^{3+}/\text{Co}^{2+}$ molar ratio of the samples, which in turn was related to a more active role of lattice oxygen in the reaction with respect to adsorbed species [20,26,44]. The relative abundance of these catalytically active species (easily reducible Co^{3+}) was optimised for the CC sample prepared by precipitation.

3.2. Characterisation of supported $\text{Co}_3\text{O}_4/\text{Al}_2\text{O}_3$ catalysts

The textural properties (BET surface area, mean pore diameter and pore volume) and Co loading of the supported $\text{Co}_3\text{O}_4/\text{Al}_2\text{O}_3$ samples ($x\text{Co}/\text{Al}_2\text{O}_3$) are shown in Table 3. The results indicated that the cobalt species deposited over the surface of the support progressively blocked its pores with increasing metallic loading, as pointed out by the observed decrease in the surface area from $136 \text{ m}^2 \text{ g}^{-1}$ for the bare γ -

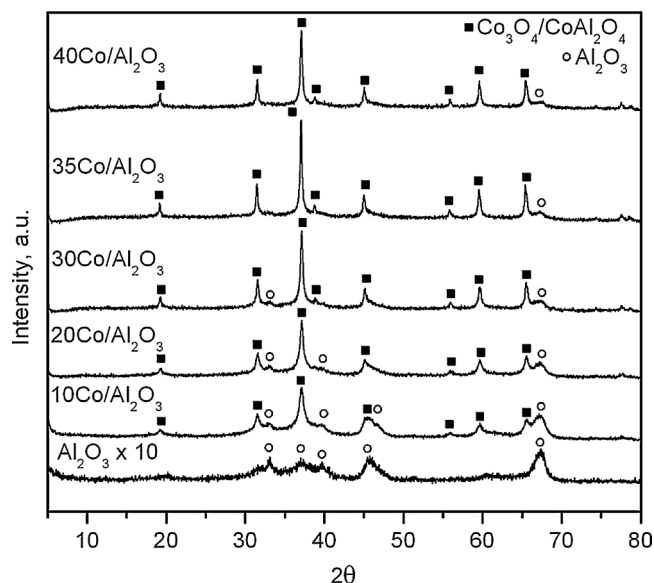


Fig. 5. XRD patterns of the $x\text{Co}/\text{Al}_2\text{O}_3$ catalysts.

alumina to $84 \text{ m}^2 \text{ g}^{-1}$ for the $40\text{Co}/\text{Al}_2\text{O}_3$ catalyst. All samples presented a lower pore volume with respect to the support, and this slightly decreased with Co loading. Furthermore, as can be seen in Fig. S3 (Supplementary material), all samples exhibited a pore size distribution centred at a smaller size in comparison with the pure $\gamma\text{-Al}_2\text{O}_3$. This suggested that the addition of cobalt to the alumina gradually blocked its largest pores.

The XRD patterns of the alumina supported Co_3O_4 catalysts are shown in Fig. 5. For the sake of comparison the patterns of the bare alumina support is also included. The following signals located at $2\theta = 19.0^\circ, 31.3^\circ, 36.8^\circ, 44.8^\circ, 59.4^\circ$ and 65.2° were clearly visible. These could, in principle, be assigned to the Co_3O_4 phase. However, the presence of CoAl_2O_4 could not be ruled out since its diffraction signals are virtually identical to those of Co_3O_4 . On the other hand, the signals of the support ($2\theta = 33.0^\circ, 37.1^\circ, 39.7^\circ, 45.6^\circ$ and 67.3°) were also observed, more noticeably in the samples with a Co loading between 10 and 30%wt. On the other hand, it was clear that the crystallinity of the samples increased with the Co loading since the diffraction signals became sharper. This, in turn, would mean that the Co_3O_4 crystallites became larger with Co loading, but their size could not be properly estimated due to the possible interference of the CoAl_2O_4 diffraction signals. However, an attempt was made to calculate the average crystallite size of the Co-phases with a spinel structure (Co_3O_4 or CoAl_2O_4). For this calculation the most intense peak of both phases ($2\theta = 36.8^\circ$) was not used since it overlapped with one signal assignable to the γ -alumina support ($2\theta = 37.1^\circ$). Accordingly, the signal at $2\theta = 59.4^\circ$ was selected for this estimation. The calculated values evidenced that crystallite size gradually increased from 13 to 35 nm with Co loading up to 35%wt. No further increase was noticed for the sample with the highest metal loading (34 nm).

The structure of the samples was additionally investigated by

Table 3
Physicochemical characterisation of $x\text{Co}/\text{Al}_2\text{O}_3$ catalysts.

Catalyst	% Co	$S_{\text{BET}}, \text{m}^2 \text{ g}^{-1}$	$V_p, \text{cm}^3 \text{ g}^{-1}$	$D_p, \text{\AA}$	$D_{\text{Co-phase}}, \text{nm}$	Low-temperature H_2 uptake, mmol g^{-1}	High-temperature H_2 uptake, mmol g^{-1}	% Co as Co_3O_4	% Co as CoAl_2O_4
$\gamma\text{-Al}_2\text{O}_3$	–	136	0.55	123	–	–	–	–	–
$10\text{Co}/\text{Al}_2\text{O}_3$	9.0	138	0.32	74	13	0.23	1.37	1.0	8.0
$20\text{Co}/\text{Al}_2\text{O}_3$	21.7	120	0.34	94	16	1.75	2.35	7.7	14.0
$30\text{Co}/\text{Al}_2\text{O}_3$	27.9	108	0.29	89	29	3.11	2.40	13.7	14.2
$35\text{Co}/\text{Al}_2\text{O}_3$	33.1	95	0.23	82	35	4.62	2.28	20.0	13.1
$40\text{Co}/\text{Al}_2\text{O}_3$	40.5	84	0.23	90	34	6.36	2.37	27.0	13.5

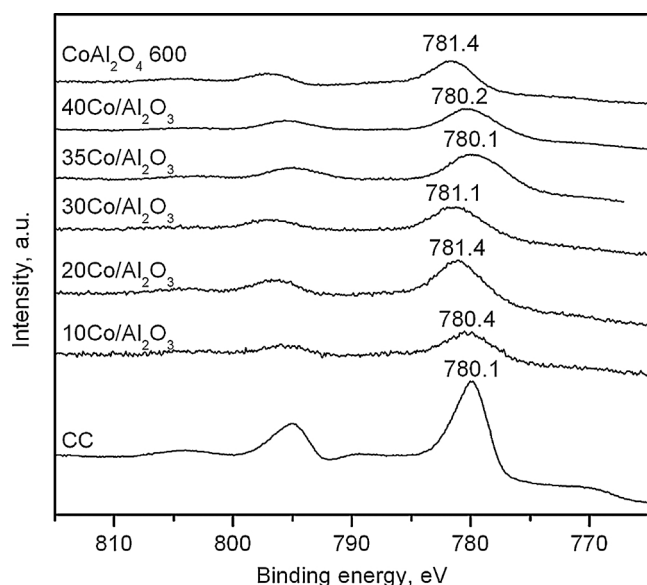


Fig. 6. XPS profiles of the xCo/Al₂O₃ catalysts.

UV–vis–NIR diffuse reflectance spectroscopy. For comparative purposes two bulk cobalt aluminate samples prepared by precipitation and calcined at 600 and 850 °C were used. The spectra of these samples along with those corresponding to the supported catalysts are shown in Fig. S4 (Supplementary material). For all the samples the spectra displayed three absorption bands located at 1210, 1320 and 1510 nm, consistent with tetrahedral Co²⁺ species, along with weak bands at 430 and 720 nm consistent with octahedral Co³⁺ species, both associated with free Co₃O₄ [45,46]. In addition, a set of bands at 552, 585 and 630 nm, related to the presence of CoAl₂O₄, was visible in the spectra of the 10Co/Al₂O₃ and 20Co/Al₂O₃ samples [46,47]. This finding suggested that both Co₃O₄ and CoAl₂O₄ were present in the supported catalysts. Also, the samples with a low Co content exhibited a band at 1930 nm associated with hydrated alumina [48].

The XPS spectra of the supported samples were characterised by a lower signal/noise ratio than that exhibited by bulk Co₃O₄. Hence, the deconvolution of these profiles was not possible. Nevertheless, the position of the main signal of the Co 2p spectra (Fig. 6) could give some information about the nature of the cobalt species on the surface. The binding energy of the 10Co/Al₂O₃, 20Co/Al₂O₃ and 30Co/Al₂O₃ catalysts increased from 780.4 to 781.1–781.4 eV, thereby revealing that CoAl₂O₄ and Co₃O₄ coexisted on the surface, in line with the results obtained by diffuse reflectance spectroscopy. Note that the main signal of the Co 2p spectra in the bulk CoAl₂O₄ sample calcined at 600 °C is located at 781.4 eV. By contrast, for the catalysts with a higher cobalt loading (35Co/Al₂O₃ and 40Co/Al₂O₃) the main signal (780.1–780.2 eV) was closer to that of the bulk Co₃O₄ (780.1 eV). This indicated that Co₃O₄ was the most abundant phase on the surface [49].

The redox properties were investigated by temperature-programmed reduction with hydrogen. The resulting profiles are included in Fig. 7. It is worth pointing out that all cobalt species present in the catalysts were completely reduced to metallic Co. This was verified by XRD analysis of the samples recovered after the TPR run since only metallic Co and Al₂O₃ were detected (Fig. S5, Supplementary material). Two main H₂ uptakes were clearly distinguished. The first contribution, located at about 250–450 °C, could be assigned to reduction of free Co₃O₄. This consumption could be in turn subdivided into other two with peak reduction temperatures at 310 and 380–440 °C, following the same reduction steps as for the bulk Co₃O₄ catalysts. Note that, unlike the bulk CC sample, the sequential reduction Co³⁺ → Co²⁺ → Co⁰ was less discernible. The second main uptake, centred at higher temperatures (660–730 °C), could be related to Co species with a substantially

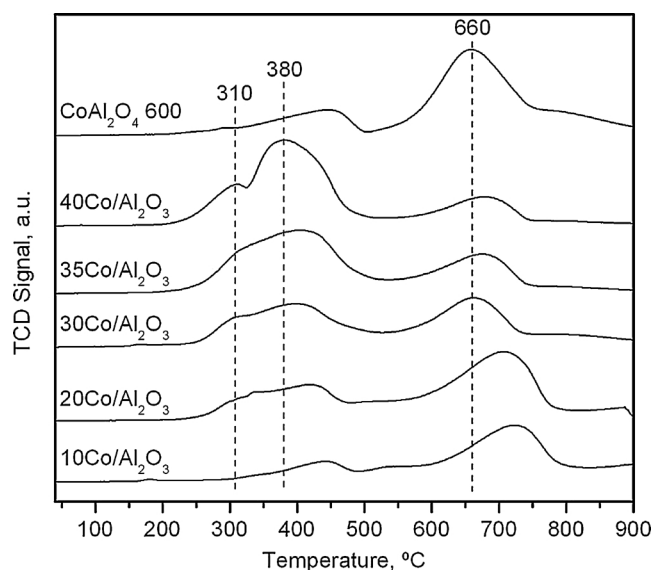


Fig. 7. H₂-TPR profiles of the xCo/Al₂O₃ catalysts.

lower reducibility. In the literature there is still a debate on the nature of this contribution since it could be attributed to either the formation of cobalt aluminate CoAl₂O₄ [46,50], or to strong interactions between Co species and the alumina support [26,51]. In an attempt to shed some light on the origin of this contribution, a H₂-TPR analysis of the bulk cobalt aluminate calcined at 600 °C was performed in order to serve as a reference for comparison with the supported catalysts. Its corresponding profile included in Fig. 7 was similar to those of the alumina supported catalysts. Thus, a low H₂ consumption was noticed at about 450 °C, which corresponded to the reduction of cobalt species (probably Co₃O₄) not fully incorporated into the lattice of CoAl₂O₄. Above 600 °C the full reduction of CoAl₂O₄ took place. Accordingly, the measured overall H₂ uptake (6.49 mmol H₂ g^{−1}) was slightly higher than the theoretical value for pure CoAl₂O₄ (5.65 mmol H₂ g^{−1}). Therefore, the comparison between the profiles of the alumina supported catalysts and that of the bulk CoAl₂O₄ sample evidenced that the high-temperature H₂ consumption observed on the supported Co₃O₄ samples could be assigned to the presence of varying amounts of cobalt aluminate. Note that the shoulder at about 900 °C observed in the profile of the 20Co/Al₂O₃ catalyst was due to an instrumental artifact involving the application of the heating ramp of the experiment. Occasionally, when the temperature were close (about 10 °C lower) to the temperature limit of the run (in this case, 900 °C), the furnace would stop heating. Then the ongoing reduction process underwent a sudden halt that resulted in that small sharp peak, which had no meaning on the redox properties of the sample.

The quantitative integration of the profiles (Table 3) revealed that the overall H₂ uptake of the 10Co/Al₂O₃ and 20Co/Al₂O₃ catalysts was very close to that expected when assuming that all cobalt species were present as CoAl₂O₄. By contrast, the observed uptake for the 35Co/Al₂O₃ and 40Co/Al₂O₃ samples was comparable with that theoretically predicted for the exclusive presence of Co₃O₄. Based on the corresponding H₂ consumption at 250–450 °C and 600–800 °C the relative distribution of Co species between Co₃O₄ and CoAl₂O₄ could be estimated for each sample. It was found that cobalt aluminate was the principal phase over the catalyst with the lowest loading (10Co/Al₂O₃). When increasing the metal content up to 20 wt% the amount of both species increased. It therefore seemed that the previously formed CoAl₂O₄ layer grew. However, above this Co concentration (30Co/Al₂O₃, 35Co/Al₂O₃ and 40Co/Al₂O₃ samples) the amount of metal as CoAl₂O₄ remained constant around 13–14 wt.%, irrespective of the cobalt loading. It could be then reasonably believed that the formed Co₃O₄ crystallites were located on top of this aluminate layer, and in

Table 4
Textural and structural properties of xCe/Co₃O₄ catalyst.

Catalyst	S _{BET} , m ² g ⁻¹	V _p , cm ³ g ⁻¹	D _p , Å	D _{Co₃O₄} , nm	Ce/Co molar ratio	Co ₃ O ₄ cell size, Å
CC	14	0.09	257	63	0	8.0958
5Ce/Co ₃ O ₄	33	0.14	155	32	0.033 (0.030)	8.0980
10Ce/Co ₃ O ₄	35	0.14	143	29	0.063 (0.064)	8.0982
15Ce/Co ₃ O ₄	30	0.11	176	38	0.100 (0.101)	8.0948
20Ce/Co ₃ O ₄	34	0.11	153	35	0.142 (0.143)	8.0940
CeO ₂	12	0.05	235	–	–	–

Values in brackets correspond to the nominal Ce/Co molar ratios.

principle, did not further converted into aluminate. This assumption was coherent with the larger H₂ uptake required for the reduction of free Co₃O₄ over these samples.

3.3. Characterisation of Ce-doped Co₃O₄ bulk catalysts

The textural and structural properties of the bulk Ce-doped Co₃O₄ (xCe/Co₃O₄) samples along with the CC sample and pure CeO₂ (for reference) are shown in Table 4. The specific surface area of Ce-doped catalysts varied between 30 and 35 m² g⁻¹, which was more than twice that of the surface area of the CC sample, while the pore volume increased by 50% approximately and the pore diameter decreased by the same amount, thus demonstrating that the addition of Ce to the bulk Co₃O₄ could improve its textural properties.

The xCe/Co₃O₄ samples showed the various diffraction signals of the cubic Co₃O₄ but slightly shifted from their positions with respect to the pure spinel (Fig. 8). In addition, the crystallite size significantly decreased from 63 to 29–38 nm. On the other hand, the samples with a Ce loading of 15 and 20 wt% also exhibited signals (2θ = 28.8°, 33.3°, 47.7°, 56.6°, 59.4°, 69.6°, 76.9° and 79.3°) related to segregated cubic fluorite-like CeO₂ (JCPDS 00-034-0394). These evidences pointed out that the addition of Ce caused a distortion in the spinel structure, which in turn decreased the Co₃O₄ crystallite size and increased the unit cell size, but only for the Ce loadings of 5 and 10%wt., as can be seen in Fig. S6 (Supplementary material). These effects have also been reported by other authors [52,53], with the latter being attributed to the larger ionic radius of Ce⁴⁺ (101 pm) in comparison with Co²⁺ (79 pm) and Co³⁺ (69 pm). The upper limit for the amount of cerium atoms that could be inserted into the lattice of Co₃O₄ seemed to be close to 10%wt. Above this loading, excess of cerium led to the formation of segregated

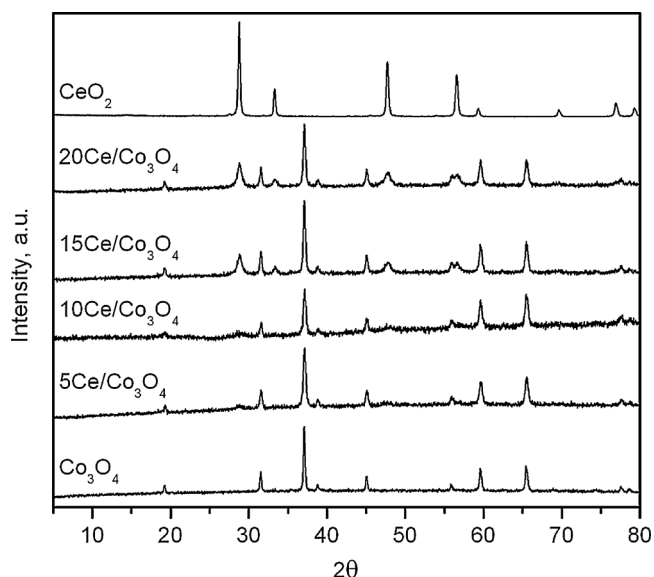


Fig. 8. XRD patterns of the xCe/Co₃O₄ catalysts.

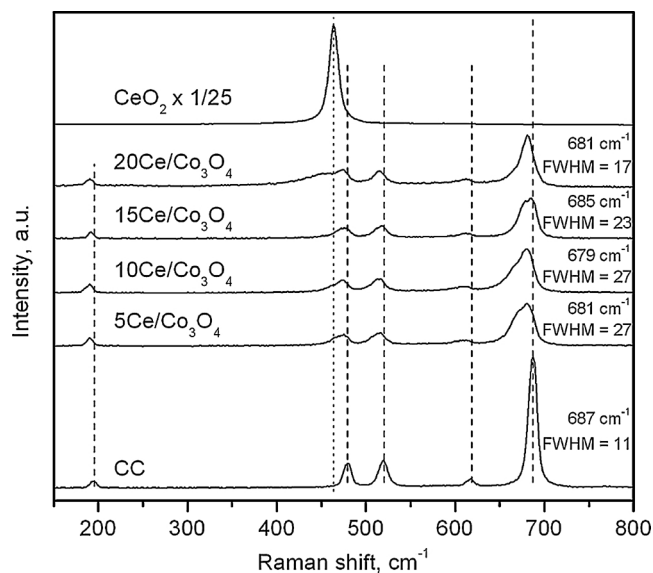


Fig. 9. Raman spectra of the xCe/Co₃O₄ catalysts.

CeO₂.

To further assess the distortion caused by the insertion of Ce atoms into the lattice of the Co₃O₄ spinel, Raman spectrometry was applied to all Ce-doped samples. The resulting spectra are included in Fig. 9. The doped oxides displayed the same five Raman bands also observed for the pure Co₃O₄, but shifted from their original positions and with broader shapes, thus suggesting the distortion of the Co₃O₄ lattice. Hence, the bands located at 194, 519 and 617 cm⁻¹ could be assigned to the F_{2g} mode, while the bands at 479 and 687 cm⁻¹ could be assigned to the E_g and A_{1g} modes, respectively [13]. Pure CeO₂, however, only displayed a markedly intense signal, located at 462 cm⁻¹, attributable to the symmetrical stretching of CeO₈ units [54]. The xCe/Co₃O₄ samples also exhibited much weaker forms of this signal, also shifted from its original position. This pointed out that the segregated CeO₂ in the 15Ce/Co₃O₄ and 20Ce/Co₃O₄ samples could also present some degree of distortion on its own lattice. The band related to the A_{1g} mode showed a much broader shape for the Ce-doped samples, with relatively higher FWHM values between 17 and 27 cm⁻¹ in comparison with the pure cobalt oxide (11 cm⁻¹). The highest values were noted over the samples 5Ce/Co₃O₄ and 10Ce/Co₃O₄, thereby pointing out that the largest extent of lattice distortion occurred in these catalysts. Accordingly, these were the samples that presented the largest cell size.

The XPS analysis of Ce-doped samples also helped in determining the role of Ce and its eventual influence on the valence changes of cobalt species. The spectra of all xCe/Co₃O₄ samples were fitted with ten peaks corresponding to five pairs of spin-orbit doublets. Following the convention adopted by Romeo et al. [55], letters U and V were used to refer to the 3d_{5/2} and 3d_{3/2} spin-orbit components, respectively. From the five pairs of peaks, three of them (namely V,U; V',U' and V'',U'') were associated with electrons from Ce⁴⁺ while the remaining pairs (V₀,U₀ and V',U') were attributed to electrons from Ce³⁺ species. As an example, the fitted Ce3d spectrum of the 10Ce/Co₃O₄ sample is shown in Fig. S7 (Supplementary material).

The Ce³⁺/Ce⁴⁺ molar ratios were obtained from the areas of both 3d_{5/2} and 3d_{3/2} components for each species. These calculated ratios were correlated with the molar Co³⁺/Co²⁺ ratios calculated from the respective Co2p spectra, as shown in Fig. 10. An inverse relationship was found, which could be explained in terms of the equilibrium Ce³⁺ + Co³⁺ ⇌ Ce⁴⁺ + Co²⁺, established by the requirement of charge balance within the cations of the spinel lattice [56,57]. An increase in Co³⁺ population at the cost of Co²⁺ resulted in a decrease of Ce³⁺ ions in favour of Ce⁴⁺.

The redox properties of the Ce-doped catalysts were investigated by

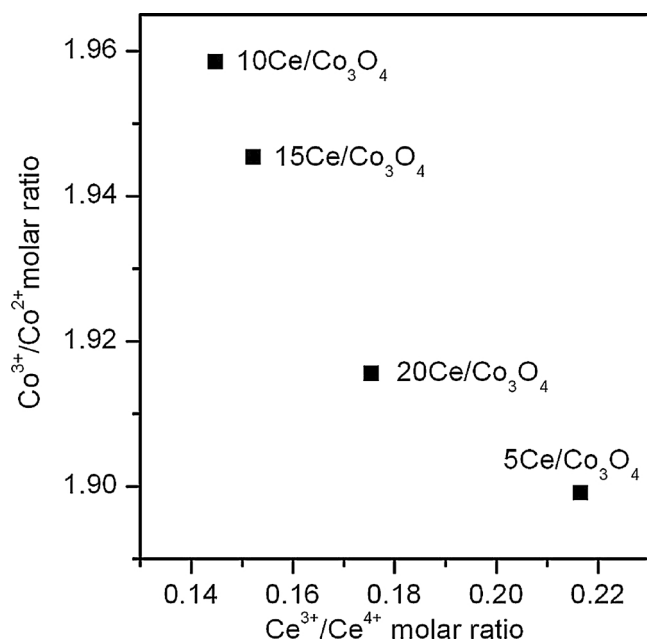


Fig. 10. Relationship between $\text{Co}^{3+}/\text{Co}^{2+}$ and $\text{Ce}^{3+}/\text{Ce}^{4+}$ molar ratios of the $\text{xCe}/\text{Co}_3\text{O}_4$ catalysts.

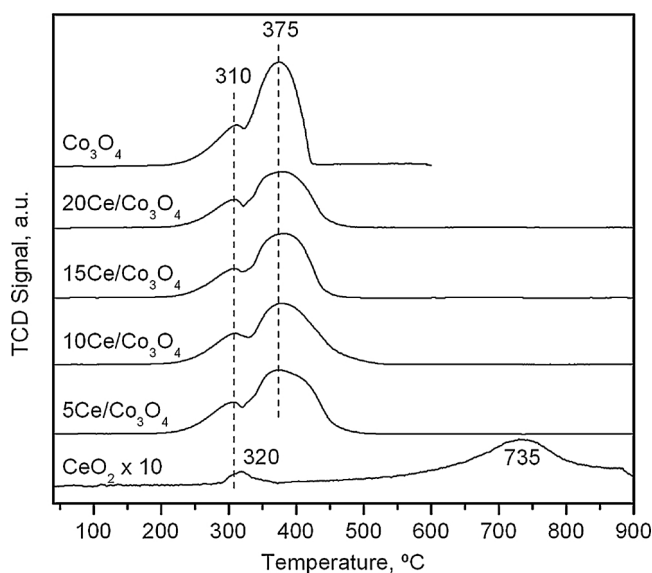


Fig. 11. H_2 -TPR profiles of the $\text{xCe}/\text{Co}_3\text{O}_4$ catalysts.

temperature-programmed reduction with hydrogen (H_2 -TPR) and temperature-programmed reaction with methane (CH_4 -TPRe). The corresponding H_2 -TPR profiles are included in Fig. 11. The hydrogen consumption profiles of the $\text{xCe}/\text{Co}_3\text{O}_4$ catalysts were similar to those

displayed by the bulk $\text{CC Co}_3\text{O}_4$, showing the same two-step reduction process, with peak temperatures at 310 and 375 °C. Note that the second reduction peak, assigned to the reduction of Co^{2+} ions, was characterised by a broader temperature window with respect to the pure cobalt oxide, probably due to the distortion caused by the insertion of Ce atoms into the spinel lattice. The reduction profile of CeO_2 also exhibited a two-step reduction process, where the first step, centred at about 320 °C, is usually attributed to the reduction of the surface while the second one, located at 735 °C, is assigned to the reduction of the bulk [58]. However, the intensity of these reduction events was substantially lower than for the reduction of Co_3O_4 , and none of the Ce-doped catalysts revealed signals of CeO_2 reduction in their TPR profiles, presumably owing to the low amount of free CeO_2 present in the samples. The results included in Table 5 pointed out that Ce doping did not result in a relevant variation of the relative H_2 uptake at low and high temperature corresponding to the reduction of the spinel.

Since the investigation of the redox properties of the $\text{xCe}/\text{Co}_3\text{O}_4$ oxides by H_2 -TPR did not evidence marked differences among the various samples, a new attempt was made by substituting H_2 by CH_4 . This change could provide more useful insights on the characterisation and identification of the available oxygen species for methane oxidation. The exit stream of the CH_4 -TPRe experiment was analysed by mass spectrometry. Thus, the $m/z = 44$ (CO_2) and the $m/z = 28$ (CO) signals were monitored. The evolution of these two species with the temperature for all $\text{xCe}/\text{Co}_3\text{O}_4$ catalysts and the CC sample are shown in Fig. 12.

Over all samples the formation of CO_2 occurred at 350–550 °C and 600–700 °C. At lower temperatures the generation was assigned to the oxidation of methane by oxygen species associated with Co^{3+} ions. At higher temperatures the CO_2 production was attributed to the oxidation of methane by oxygen species associated with Co^{2+} ions [59]. However, as opposed to the H_2 -TPR profiles, the temperature windows for both reactions were clearly discernible. In all cases, the formation of CO_2 at high temperatures was also accompanied by the generation of CO and H_2 to some extent. This could be due to the ability of Co^{2+} ions to catalyse the reforming of methane as well [60] and also due to the deficit of oxygen present in the catalysts after all Co^{3+} ions were reduced. Both CO_2 contributions took the shape of definite non-Gaussian peaks. Interestingly, for the 10Ce/ Co_3O_4 sample, the formation of CO_2 occurred at significantly lower temperatures (460 and 605 °C) when compared with the CC sample (485 and 620 °C). Each CH_4 -TPRe experiment was followed by a H_2 -TPR analysis to check if methane could completely reduce the catalysts. No hydrogen uptake was found, thereby evidencing that all samples were completely reduced by methane. Integration and quantification of the CO_2 production at low and high temperatures (Table 5) revealed a better behaviour for the conversion of CH_4 at low temperatures over the 10Ce/ Co_3O_4 sample. These results demonstrated that the addition of small amounts of Ce to bulk Co_3O_4 catalysts improved their ability for methane oxidation.

3.4. Comparison between $\text{Co}_3\text{O}_4/\text{Al}_2\text{O}_3$ and Ce-doped Co_3O_4 bulk catalysts

Catalytic activity of alumina supported and Ce-doped Co_3O_4

Table 5

Results of H_2 -TPR and CH_4 -TPRe analysis of the $\text{xCe}/\text{Co}_3\text{O}_4$ catalysts.

Catalyst	H_2 -TPR			CH_4 -TPRe		
	Low-temperature peak, mmol g^{-1}	High-temperature peak, mmol g^{-1}	Relative H_2 uptake at low and high temperature	Low-temperature peak, °C	High-temperature peak, °C	Relative CO_2 production at low and high temperature
CC	4.29	12.41	0.35	485	620	0.56
5Ce/ Co_3O_4	3.80	11.38	0.33	480	680	0.54
10Ce/ Co_3O_4	3.76	10.36	0.36	460	605	0.66
15Ce/ Co_3O_4	3.42	9.68	0.35	500	675	0.61
20Ce/ Co_3O_4	3.15	9.20	0.34	510	695	0.63

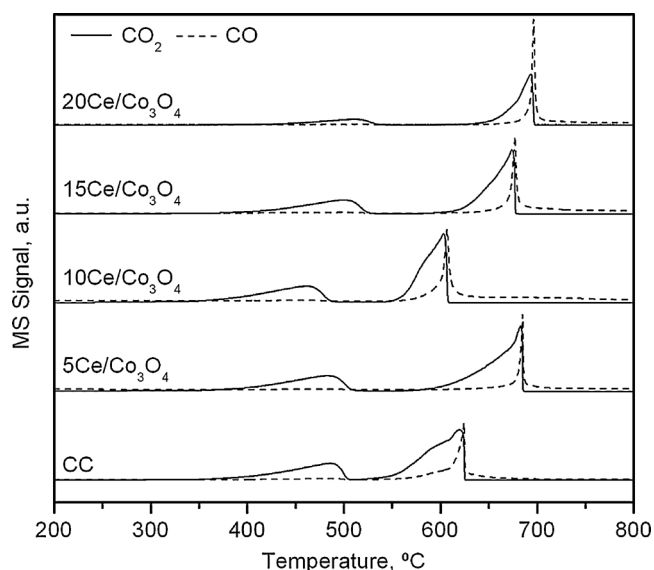


Fig. 12. CH₄-TPRe profiles of the xCe/Co₃O₄ catalysts.

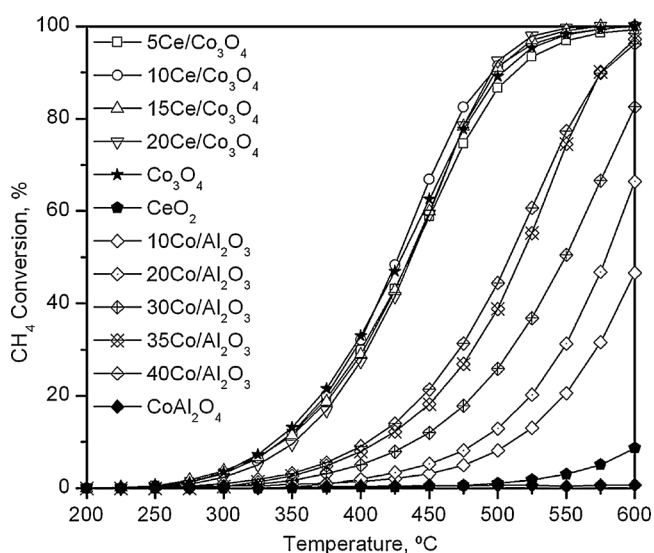


Fig. 13. Light-off curves of the xCo/Al₂O₃ and xCe/Co₃O₄ catalysts.

catalysts were examined under the same conditions as for the bulk Co₃O₄ catalysts. The corresponding light-off curves are included in Fig. 13. It was noticed that the activity of the alumina supported samples expectedly increased with Co loading, with a T₅₀ value of 515 and 510 °C over the 35Co/Al₂O₃ and 40Co/Al₂O₃ catalysts, respectively. Nevertheless, in no case their activity was higher than that of the bulk catalysts, despite exhibiting much better textural properties. This was probably due to two reasons. First, cobalt aluminate, hardly reducible at the selected reaction temperatures, fixed a great amount of the cobalt deposited, thereby decreasing the availability of potentially active cobalt species. Recall that the activity of pure CoAl₂O₄ was negligible. Secondly, as shown by the H₂-TPR profiles, the amount of easily reducible, highly active Co³⁺ in the supported catalysts was lower than that of bulk catalysts, which made free Co₃O₄ within the support less active than the bulk Co₃O₄. Similar results were obtained by other authors, for Co₃O₄/Al₂O₃ catalysts obtained by both wet [11] and incipient wetness impregnation [26].

The reaction rate estimated under differential conditions ($X < 20\%$ at 425 °C) are listed in Table 2. The highest reaction rate was found over the 35Co/Al₂O₃ catalyst (2.2 mmol CH₄ g_{Co}⁻¹ h⁻¹) followed by the 40Co/Al₂O₃ and 30Co/Al₂O₃ samples (2.1 and 1.9 mmol CH₄

g_{Co}⁻¹ h⁻¹, respectively). By contrast, both 10Co/Al₂O₃ and 20Co/Al₂O₃ samples showed a noticeably lower reaction rate, around 1.2 mmol CH₄ g_{Co}⁻¹ h⁻¹. On the other hand, a progressive decrease in the apparent activation energy with Co loading was evident. Over the catalysts with a low Co content, where CoAl₂O₄ was the most abundant phase, the activation energy was around 100 kJ mol⁻¹. For higher loadings, and more particularly over the 35Co/Al₂O₃ and 40Co/Al₂O₃ catalysts, the activation energy was close (78–79 kJ mol⁻¹) to that observed for the bulk Co₃O₄ catalyst (CC sample). These values were evaluated from the fit of experimental conversion data to the Eq. (1).

Regarding Ce-doped samples all the light-off curves were relatively similar with a T₅₀ in the 425–435 °C range. It must be pointed out that the pure CeO₂ was virtually inactive, with a conversion as low as 10% at 600 °C. Only the 10Ce/Co₃O₄ sample showed a slightly better behaviour with respect to the pure bulk Co₃O₄ catalyst. More perceptible differences were noticed when the specific reaction rates at 375 °C ($X < 20\%$) were compared. Thus, it was 2 mmol CH₄ g_{Co}⁻¹ h⁻¹ over the 10Ce/Co₃O₄ sample and 1.8 mmol CH₄ g_{Co}⁻¹ h⁻¹ over the pure cobalt oxide. This revealed that the addition of cerium had a positive effect on the specific activity of bulk Co₃O₄. It is worth pointing out that the alumina supported catalysts required temperatures at least 50 °C higher to achieve similar reaction rates. The estimated apparent activation energy of the 5Ce/Co₃O₄, 10Ce/Co₃O₄ and 15Ce/Co₃O₄ catalysts were 78–79 kJ mol⁻¹, close to the value determined for the pure counterpart. Over the 20Ce/Co₃O₄ catalyst, characterised by a considerable amount of segregated ceria, the value significantly increased up to 85 kJ mol⁻¹. Note that pure CeO₂ gave an activation energy of 108 kJ mol⁻¹. The relationship shown in Fig. 14 revealed that the specific reaction rate was clearly influenced by the mobility of the oxygen species, which was evaluated from the amount of oxygen reacting with methane at low temperatures, which corresponded to the Co³⁺ → Co²⁺ reduction step in the CH₄-TPRe run. In sum, it could be concluded that the addition of small amounts of cerium atoms, which were introduced into the lattice of Co₃O₄, resulted in an enhancement of the intrinsic activity of the spinel owing to a distortion of the crystalline structure which ultimately led to an increased population of Co³⁺, an improved reducibility and a higher mobility of the oxygen species in the spinel lattice.

The deep oxidation of methane over Ce-Co oxide catalysts has been widely investigated in the recent years. For example, Li et al. achieved a T₅₀ of 400 °C (25 °C lower than in this work) under similar reaction

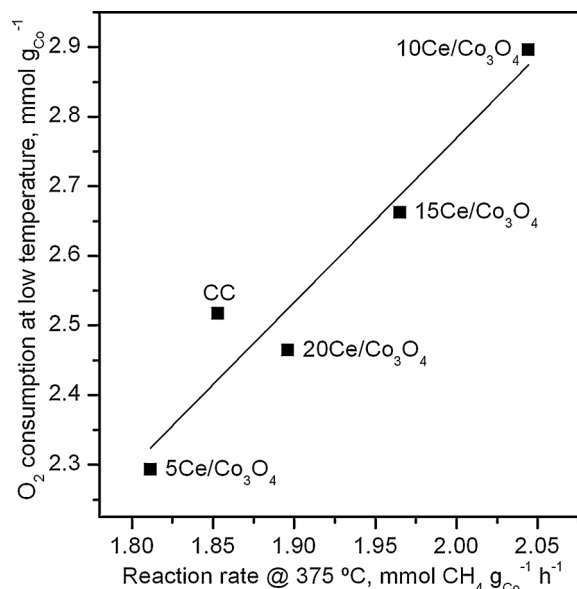


Fig. 14. Relationship between the O₂ consumption at low temperatures (CH₄-TPRe) and the specific reaction rate.

conditions over a Ce-Co catalyst prepared by a sol-gel method [28]. Vickers et al. obtained comparable results (T_{50} around 400 °C) using CeO_2 supported over a meso- Co_3O_4 obtained using KIT-6 as hard template but operating at 180 ml $\text{CH}_4 \text{ g}^{-1} \text{ h}^{-1}$ [61]. In both cases, the Ce/Co molar ratio (0.33 and 0.10, respectively) used was significantly higher than in this work (0.06), which points out that the activity promoting effect of cerium in those catalysts was actually lower than that observed in this work. In addition, Liotta et al. [62] achieved a T_{50} of 455 °C (180 ml $\text{CH}_4 \text{ g}^{-1} \text{ h}^{-1}$) by using Co_3O_4 supported over CeO_2 with a Ce/Co molar ratio of 1.1. Our results therefore evidenced that active Ce-Co catalysts could be designed with a relatively low Ce content. Finally, attention was also paid to examining the stability of the most active catalysts, namely 10Ce/ Co_3O_4 and CC samples, when operating at constant temperature (450 °C) during a relatively prolonged time (150 h). The results included in Fig. S8 (Supplementary material) revealed that both oxides gave a relatively stable conversion close to 75%, although the cerium-free sample showed a slight instability. The characterisation of the used 10Ce/ Co_3O_4 sample by BET measurements and XRD revealed a reduced impact on its surface area ($30 \text{ m}^2 \text{ g}^{-1}$, $35 \text{ m}^2 \text{ g}^{-1}$ for the fresh sample) and crystallite size (30 nm, 29 nm for the fresh sample).

Given the reasonably good results achieved by the 10Ce/ Co_3O_4 catalyst its stability at 425 °C was also evaluated under humid conditions (in the presence of 5% H_2O) for 150 h. The results are also shown in Fig. S8 (Supplementary material). It was found that water noticeably decreased the catalytic performance with a reasonably constant conversion around 40%. The surface area after this run decreased to $24 \text{ m}^2 \text{ g}^{-1}$ in line with the concomitant enlargement of the crystallite size (35 nm). This used sample was further submitted to an additional stability test under dry conditions for 20 h (Fig. S8, Supplementary material). It was noticed that conversion was not fully recovered, but it was still around 65%. This finding certainly evidenced that water, apart from inhibiting the catalytic activity by competitive effects, also had a significant negative effect on the physicochemical properties of the sample [17,63].

4. Conclusions

The performance of three type of Co_3O_4 catalysts, namely bulk, alumina-supported and Ce-doped samples, was examined for the combustion of methane under similar reaction conditions to those in the exhaust gas of VNG engines. The activity of bulk catalysts was found to be controlled by an increased $\text{Co}^{3+}/\text{Co}^{2+}$ molar ratio that in turn evidenced a more active role of surface lattice oxygen in the reaction. Higher reaction rates were achieved by Co_3O_4 catalysts prepared by basic aqueous precipitation. Interestingly, the addition of a relatively small amount of cerium (10%wt.) to the Co_3O_4 lattice led to an increase in the inherent catalytic activity of the cobalt phase due to an improvement in the mobility of lattice oxygen species associated with easily reducible Co^{3+} ions. This optimised catalyst exhibited a marked stability under both dry and humid conditions during a relatively prolonged reaction time. On the other hand, owing to the notable negative impact induced by cobalt aluminate formation, the behaviour of alumina supported catalysts was shown to be inferior with respect to the bulk samples. As a result, notable conversion levels were only attained with a Co loading higher than 30%wt.

Acknowledgements

The author wish to thank the financial support provided by the Ministry of Economy and Competitiveness (CTQ2016-80253-R), Basque Government (IT657-13) and the University of the Basque Country UPV/EHU, and the technical and human support provided by SGiker (UPV/EHU) and the University of Cádiz.

Appendix A. Supplementary data

Supplementary material related to this article can be found, in the online version, at doi:<https://doi.org/10.1016/j.apcatb.2018.06.050>.

References

- [1] M.I. Jahirul, H.H. Masjuki, R. Saidur, M.A. Kalam, M.H. Jayed, M.A. Wazed, *Appl. Therm. Eng.* 30 (2010) 2219–2226.
- [2] M. Hussain, F.A. Deorsola, N. Russo, D. Fino, R. Pirone, *Fuel* 149 (2015) 2–7.
- [3] S. Di Pascoli, A. Femia, T. Luzzati, *Ecol. Econ.* 38 (2001) 179–189.
- [4] T. Korakianitis, A.M. Namasivayam, R.J. Crookes, *Prog. Energy Combust.* 37 (2011) 89–112.
- [5] Z. Li, G.B. Hoflund, *J. Nat. Gas Chem.* 12 (2003) 153–160.
- [6] J.K. Lampert, M.S. Kazi, R.J. Farrauto, *Appl. Catal. B Environ.* 14 (1997) 211–223.
- [7] Q. Xu, K.C. Kharas, B.J. Croley, A.K. Datye, *ChemCatChem* 3 (2011) 1004–1014.
- [8] L.S. Escandón, D. Niño, E. Díaz, S. Ordóñez, F.V. Díez, *Catal. Commun.* 9 (2008) 2291–2296.
- [9] S. Ordóñez, J.R. Paredes, F.V. Díez, *Appl. Catal. A Gen.* 341 (2008) 174–180.
- [10] A. Setiawan, E.M. Kennedy, B.Z. Dlugogorski, A.A. Adesina, M. Stockenhuber, *Catal. Today* 258 (2015) 276–283.
- [11] T. Xiao, S. Ji, H. Wang, K.S. Coleman, M.L.H. Green, *J. Mol. Catal. A Chem.* 175 (2001) 111–123.
- [12] J. Chen, H. Arandiyán, X. Gao, J. Li, *Catal. Surv. Asia* 19 (2015) 140–171.
- [13] Q. Liu, L. Wang, M. Chen, Y. Cao, H. He, K. Fan, *J. Catal.* 263 (2009) 104–113.
- [14] G. Salek, P. Alphonse, P. Dufour, S. Guillemet-Fritsch, C. Tenailleau, *Appl. Catal. B Environ.* 147 (2014) 1–7.
- [15] Q. Ren, S. Mo, R. Peng, Z. Feng, M. Zhang, L. Chen, M. Fu, J. Wu, D. Ye, J. Mater. Chem. A 6 (2018) 498–509.
- [16] J. González-Prior, R. López-Fonseca, J.I. Gutiérrez-Ortiz, B. de Rivas, *Appl. Catal. B Environ.* 222 (2018) 9–17.
- [17] L.F. Liotta, G. Di Carlo, G. Pantaleo, A.M. Venezia, G. Deganello, *Appl. Catal. B Environ.* 66 (2006) 217–227.
- [18] N. Bahlawane, *Appl. Catal. B Environ.* 67 (2006) 168–176.
- [19] Y. Ji, Z. Zhao, A. Duan, G. Jiang, J. Liu, *J. Phys. Chem. C* 113 (2009) 7186–7199.
- [20] N. Bahlawane, P.H.T. Ngamou, V. Vannier, T. Kottke, J. Heberle, K. Kohse-Höinghaus, *Phys. Chem. Chem. Phys.* 11 (2009) 9224–9232.
- [21] Z. Tian, P.H. Tchoua Ngamou, V. Vannier, K. Kohse-Höinghaus, N. Bahlawane, *Appl. Catal. B Environ.* 117–118 (2012) 125–134.
- [22] N. van Vegten, T. Baidya, F. Krumeich, W. Kleist, A. Baiker, *Appl. Catal. B Environ.* 97 (2010) 398–406.
- [23] Z. Chen, S. Wang, W. Liu, X. Gao, D. Gao, M. Wang, S. Wang, *Appl. Catal. A Gen.* 525 (2016) 94–102.
- [24] Z. Pu, H. Zhou, Y. Zheng, W. Huang, X. Li, *Appl. Surf. Sci.* 410 (2017) 14–21.
- [25] U. Zavyalova, P. Scholz, B. Ondruschka, *Appl. Catal. A Gen.* 323 (2007) 226–233.
- [26] Q. Wang, Y. Peng, J. Fu, G.Z. Kyzas, S.M.R. Billah, S. An, *Appl. Catal. B Environ.* 168–169 (2015) 42–50.
- [27] N.E. Machin, C. Karakaya, A. Celepci, *Energy Fuel* 22 (2008) 2166–2171.
- [28] H. Li, G. Lu, D. Qiao, Y. Wang, Y. Guo, Y. Guo, *Catal. Lett.* 141 (2011) 452–458.
- [29] M. Kumar, G. Rattan, R. Prasad, *Can. Chem. Trans.* 3 (2015) 381–409.
- [30] B. de Rivas, R. López-Fonseca, C. Jiménez-González, J.I. Gutiérrez-Ortiz, *J. Catal.* 281 (2011) 88–97.
- [31] A.A. Mirzaei, H.R. Shaterian, R.W. Joyner, M. Stockenhuber, S.H. Taylor, G.J. Hutchings, *Catal. Commun.* 4 (2003) 17–20.
- [32] Eurokin. <http://eurokin.org/>, 2018 (Accessed 20 February 2018).
- [33] A. Aranzabal, J.A. González-Marcos, J.L. Ayastuy, J.R. González-Velasco, *Chem. Eng. Sci.* 61 (2006) 3564–3576.
- [34] C. Shi, Y. Wang, A. Zhu, B. Chen, C. Au, *Catal. Commun.* 28 (2012) 18–22.
- [35] A. Biabani-Ravandi, M. Rezaei, *Chem. Eng. J.* 184 (2012) 141–146.
- [36] S. Arnone, G. Bagnasco, G. Busca, L. Lisi, G. Russo, M. Turco, *Stud. Surf. Sci. Catal.* 119 (1998) 65–70.
- [37] J. González-Prior, R. López-Fonseca, J.I. Gutiérrez-Ortiz, B. de Rivas, *Appl. Catal. B Environ.* 199 (2016) 384–393.
- [38] S.A. Singh, G. Madras, *Appl. Catal. A Gen.* 504 (2015) 463–475.
- [39] M.C. Biesinger, B.P. Payne, A.P. Grosvenor, L.W.M. Lau, A.R. Gerson, R.S.C. Smart, *Appl. Surf. Sci.* 257 (2011) 2717–2730.
- [40] J. Dupin, D. Gonbeau, P. Vinatier, A. Levasseur, *Phys. Chem. Chem. Phys.* 2 (2000) 1319–1324.
- [41] P. Stefanov, S. Todorova, A. Naydenov, B. Tzaneva, H. Kolev, G. Atanasova, D. Stoyanova, Y. Karakirova, K. Aleksieva, *Chem. Eng. J.* 266 (2015) 329–338.
- [42] G.I. Golodets, V. Chapter, The kinetics of gas-phase heterogeneous catalytic reactions involving molecular oxygen, in: G.I. Golodets (Ed.), *Heterogeneous Catalytic Reactions Involving Molecular Oxygen*, Elsevier, Amsterdam, 1983, pp. 126–150.
- [43] J.R. Paredes, E. Díaz, F.V. Díez, S. Ordóñez, *Energy Fuel* 23 (2009) 86–93.
- [44] J. Li, X. Liang, S. Xu, J. Hao, *Appl. Catal. B Environ.* 90 (2009) 307–312.
- [45] Y. Brik, M. Kacimi, M. Ziyad, F. Bozon-Verduraz, *J. Catal.* 202 (2001) 118–128.
- [46] L.G.A. van de Water, G.L. Bezemer, J.A. Bergwerff, M. Versluijs-Helder, B.M. Weckhuysen, K.P. de Jong, *J. Catal.* 242 (2006) 287–298.
- [47] T. Das, S. Sengupta, G. Deo, *React. Kinet. Mech. Catal.* 110 (2013) 147–162.
- [48] F. Dumond, E. Marceau, M. Che, *J. Phys. Chem. C* 111 (2007) 4780–4789.
- [49] X. Duan, M. Pan, F. Yu, D. Yuan, *J. Alloy Compd.* 509 (2011) 1079–1083.
- [50] I. Zacharakis, C.G. Kontoyannis, S. Boghosian, A. Lycourghiotis, C. Kordulis, *Catal. Today* 143 (2009) 38–44.
- [51] B. Solsona, T.E. Davies, I. Vázquez, A. Dejoz, S.H. Taylor, *Appl. Catal. B*

- Environ. 84 (2008) 176–184.
- [52] D. Li, L. Wang, M. Koike, Y. Nakagawa, K. Tomishige, Appl. Catal. B Environ. 102 (2011) 528–538.
- [53] G. Zou, Y. Xu, S. Wang, M. Chen, W. Shanguan, Catal. Sci. Technol. 5 (2015) 1084–1092.
- [54] K.K. Babitha, A. Sreedevi, K.P. Priyanka, B. Sabu, T. Varghese, Indian J. Pure Appl. Phys. 53 (2015) 596–603.
- [55] M. Romeo, K. Bak, J. El Fallah, F. Le Normand, L. Hilaire, Surf. Interface Anal. 20 (1993) 508–512.
- [56] J. Chen, C. Li, S. Li, P. Lu, L. Gao, X. Du, Y. Yi, Chem. Eng. J. 338 (2018) 358–368.
- [57] R. Dziembaj, A. Chojnacka, Z. Piwowarska, M. Gajewska, M. Swietoslawski, S. Górecka, M. Molenda, Catal. Today (2018), <http://dx.doi.org/10.1016/j.cattod.2018.03.042>.
- [58] M. Florea, F. Matei-Rutkovska, G. Postole, A. Urda, F. Neatu, V.I. Părvulescu, P. Gelin, Catal. Today 306 (2018) 166–171.
- [59] L. Hu, Q. Peng, Y. Li, J. Am. Chem. Soc. 130 (2008) 16136–16137.
- [60] A.W. Budiman, S. Song, T. Chang, C. Shin, M. Choi, Catal. Surv. Asia 16 (2012) 183–197.
- [61] S.M. Vickers, R. Gholami, K.J. Smith, M.J. MacLachlan, ACS Appl. Mater. Inter. 7 (2015) 11460–11466.
- [62] L.F. Liotta, G. Di Carlo, G. Pantaleo, G. Deganello, Appl. Catal. B Environ. 70 (2007) 314–322.
- [63] D. Qiao, G. Lu, Y. Guo, Y. Wang, Y. Guo, J. Rare Earth 28 (2010) 742–746.